Direct numerical simulation of coflowing rough and smooth turbulent channel flows

Harish Varma,[1,2,*] Karthikeyan Jagadeesan,[1] Vagesh D. Narasimhamurthy,[1] and Amit P. Kesarkar[2]

[1]*Department of Applied Mechanics, Indian Institute of Technology Madras, Chennai 600036, India*
[2]*National Atmospheric Research Laboratory, Gadanki 517112, India*

(Received 13 June 2022; accepted 16 May 2023; published 5 June 2023)

Fully developed turbulent flows through ribbed channels have been simulated using direct numerical simulation (DNS). Square ribs were arranged transversely to the flow on one of the channel walls, and based on their spanwise extent, resulted in two configurations—two-dimensional (2D) configuration resulting from full-span-width ribs and a three-dimensional (3D) configuration, where the ribs extend only up to half the span-width of the channel, leaving the other half smooth. The 3D configuration thus produced a unique problem of coflowing rough and smooth turbulent channel flows. A striking phenomenon has been observed of the secondary roll cells, exhibiting a strong updraft in the smooth half of the channel. The mean velocity profile from the smooth half surprisingly possesses a linear region of constant slope at the channel core. Comparisons were also drawn with DNS of a smooth channel at the same friction Reynolds number 400 and it was found that the roll cells on the smooth half not only affect the bulk flow negatively but also attenuate the turbulence significantly. In spite of having a higher bulk velocity, the rough half of the 3D configuration is more turbulent than the 2D configuration; this has been attributed to the momentum transfer from the smooth half to the rough half. Statistical turbulence quantities, and the production rates of turbulent kinetic energy and enstrophy have been used to arrive at the inferences. In essence, the roll cells buffer the variations between the rough and the smooth halves in the 3D configuration. The instantaneous streamwise velocity fluctuations in the 3D configuration displayed a wavelike form.

DOI: 10.1103/PhysRevFluids.8.064602

I. INTRODUCTION

Rough-wall-bounded flows is a topic of high interest owing to its wide range of applications in industrial and atmospheric flows. In case of atmospheric boundary layer flows (ABL), the underlying surface is mostly rough, where the roughness pattern ranges from uneven terrains to ordered urban canyons. There are cities with presence of buildings and water bodies abreast, which can be a good example of boundary layer flows with underlying rough and smooth surfaces alongside each other. Preceding the current study, there are only a few studies that have investigated such transverse roughness transitions [1–3].

In the direct numerical simulation (DNS) study by Leonardi *et al.* [4], turbulent channel flows with only one wall roughened with transversely arranged square ribs was investigated. Several values of the ratio w/k were studied. Here k is the rib height and w is the cavity width between consecutive ribs. It was found that at a very high ratio of $w/k = 39$, the flow close to the cavity floor approaches the flow over a smooth wall, with the presence of streamwise elongated vorticity

*harishvarma@narl.gov.in

 ©2023 American Physical Society

structures, which alternate in sign in the spanwise direction. Another such study of rough channel flow was by Orlandi *et al.* [2] in which two-dimensional roughness elements were simulated, with a different cross-section for the roughness elements in each case. The effects of streamwise and transverse orientations of the 2D roughness elements were investigated. Drag is higher when the roughness elements are aligned in the transverse direction. In the case of streamwise orientation of the elements, the shape of roughness was observed to influence the turbulent shear stress more than the viscous stress. A continuation of this study by Orlandi and Leonardi [5] discusses the effects of three-dimensional roughness. The three-dimensional roughness was observed to have a stronger influence on the overlying flow than the two-dimensional roughness. A comparative study involving DNS and experiments was carried out by Burattini *et al.* [6], of turbulent channel flows roughened with transversely arranged square ribs on one wall. The study was carried out for several Reynolds numbers within the range $\mathrm{Re}_{\tau_r} = 300$–$1100$, where Re_{τ_r} is the Reynolds number based on the friction velocity at the rough wall and the half-height of the channel. The profiles of Reynolds normal stresses on the rough side are nearly independent of Re_{τ_r}, when normalized by outer variables.

Willingham *et al.* [1], investigated a turbulent boundary layer flow over a transverse roughness transition, using large eddy simulation (LES). The abrupt variation in the wall shear stress along the span induces transverse secondary flows leading to the formation of a so-called low momentum pathway (LMP). As per Mejia-Alvarez *et al.* [7] and Adrian *et al.* [8], LMP is possibly caused by the streamwise alignment of coherent structures into larger scale packets inducing a momentum deficit region. In the experimental study by Bai *et al.* [3], turbulent boundary layer over a rough wall with spanwise-alternating high and low roughness strips was investigated. The high and low roughness strips composed of sand paper with two different grit diameters. Secondary flows comprising large-scale counter-rotating roll cells were observed in the cross stream plane over the wall, with common-flow down toward the high roughness strip and common-flow up away from the low roughness strip, resulting in spanwise variation of boundary layer thickness and turbulence. The study highlighted the presence of streamwise-elongated and meandering velocity streaks, similar to that over a smooth-walled boundary layer. Such wavelike/meandering form of fluid flow is often observed in adjacent flows of fluids at different Reynolds numbers. In this context, two consecutive DNS studies by Narasimhamurthy *et al.* [9] and Teja *et al.* [10] investigated the onset of shear-layer instability at the interface of two parallel Couette flows, where the formation of a wave and its characteristics were exclusively studied.

In the recent study by Varma *et al.* [11], a fully developed turbulent channel flow with symmetrically roughened walls was investigated, where the channel walls were roughened with square ribs. The flow was found to be more anisotropic at friction Reynolds number $\mathrm{Re}_\tau = 180$ than at $\mathrm{Re}_\tau = 400$. "Wormlike" vortical structures were found to be closely associated with the regions of positive enstrophy production rate. The enstrophy equation for an incompressible homogeneous fluid is given by

$$\frac{D}{Dt}\left(\frac{1}{2}\omega_i^2\right) = \omega_i S_{ij}\omega_j - \nu\left(\frac{\partial \omega_i}{\partial x_j}\right)^2 + \nu\frac{\partial^2}{\partial x_j^2}\left(\frac{1}{2}\omega_i^2\right), \tag{1}$$

where the $\omega_i S_{ij}\omega_j$ term in equation (1) represents the production rate of the enstrophy. It is described as vortex stretching term, since it is the scalar product of the vorticity vector with the vorticity stretching vector, $S_{ij}\omega_j$. It represents the effects of local amplification of enstrophy by vortex filament stretching. The last two terms of the equation represent the spread of vorticity due to viscosity [12]. The vorticity stretching or compression, given by $\omega_i S_{ij}\omega_j > 0$ or $\omega_i S_{ij}\omega_j < 0$, respectively, affects the transfer process in the energy cascade, where $\omega_i S_{ij}\omega_j > 0$ enhances the transfer of turbulent energy to small scales.

The present study aims at investigating the turbulent channel flow with the underlying rough and smooth surfaces present abreast (i.e., in a side-by-side or parallel arrangement). Turbulent statistics, anisotropy, enstrophy production rate, and vortical structures derived from the DNS are

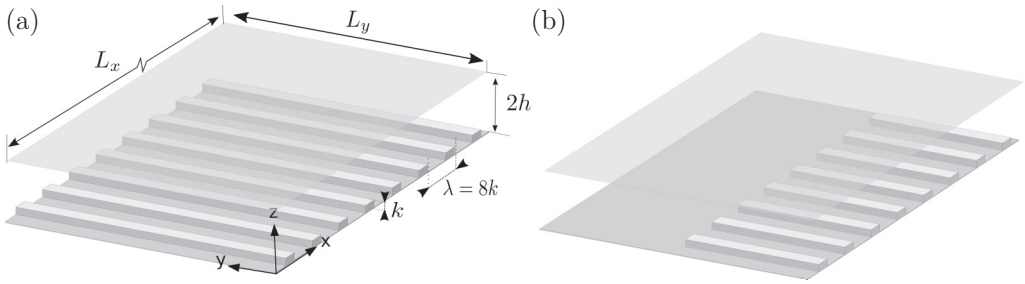

FIG. 1. Computational domain of (a) RC and (b) RSC, where $k = 0.1h$ and pitch $\lambda = 0.8h$; $L_x = 12.8h$, $L_y = 6.4h$.

used to understand the modifications in the flow dynamics due to this unique transverse roughness transition. The study also includes a DNS of channel flow with one wall entirely roughened and a DNS of smooth channel flow, which were performed to make a comparative analysis with the primary simulation. Instantaneous and mean flow features are exclusively reported over different cross section planes. The time variation of velocity fluctuations is visualized to identify any wavelike behavior of the flow.

II. FLOW SETUP AND METHODOLOGY

A. Problem definition

In the current work, fully developed flows through ribbed channels with two different rib arrangements have been studied. In the first configuration (hereafter called RC denoting rough channel), 2D square ribs are placed transverse to the flow, on one of the channel walls. In the second case (hereafter called RSC denoting "rough-smooth" channel), square ribs are similarly placed on one of the channel walls, but extending to only half the channel span, amounting to a 3D roughness configuration. Results from RSC are not only compared with those from RC, but also from DNS of a smooth channel flow (hereafter called SC). In Fig. 1, where a schematic of RC and RSC is shown, x, y, and z denote the streamwise, spanwise, and normal (to the wall) directions, respectively. The cross-section of the square ribs has a height $k = 0.1h$, where h refers to half-height of the channel and the ribs are spaced along x at a pitch $\lambda = 8k$.

In Fig. 1, L_x, L_y, and L_z refer to the extents of the computational domain in x, y, and z, respectively. While in SC, L_x and L_y are $6.4h$ and $3.2h$, respectively, in RSC and RC they are twice the former values—$12.8h$ and $6.4h$, respectively. The aforementioned choices are based on the requirement that two-point correlations of the velocity fluctuations vanish within half the chosen dimensions. The two-point correlation coefficient R_{uu} is defined as

$$R_{uu}(r_i) = \frac{\langle u(x_i, t)u(x_i + r_i, t)\rangle}{\langle u(x_i, t)u(x_i, t)\rangle},$$

where r_i denotes the displacement vector—in the case of streamwise correlation shown in Fig. 2(a), r_i denotes the separation distance in x and in the case of spanwise correlation shown in Fig. 2(b), r_i denotes the separation distance in y. The profile of two-point correlation in the spanwise direction is nearly zero at half the spanwise width. The profile of streamwise correlation is less converging to zero, which is due to the oscillations of streamwise velocity fluctuations in (x, y) plane, manifesting into a wavelike form, as detailed in Sec. III D. For the chosen values of L_x, k, and λ, RC and RSC accommodates 16 ribs. The flow is driven by a constant mean pressure gradient in x, $\Delta P/\Delta x = -1$. According to the mean momentum balance in x, the imposed pressure gradient balances both the viscous shear stress at the channel walls and the pressure drop arising across the ribs. Hence, the

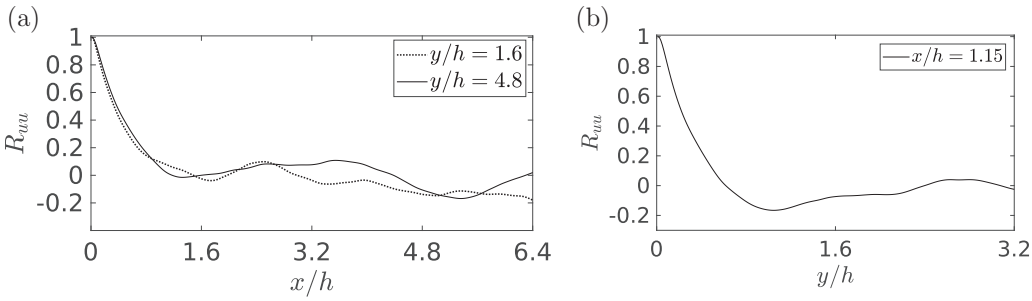

FIG. 2. Two-point correlations of the streamwise velocity fluctuations u from RSC in (a) streamwise and (b) spanwise directions at $z/h = 1.0$.

average friction velocity u_τ was obtained as

$$u_\tau = \left(-\frac{h}{\rho}\frac{\Delta P}{\Delta x}\right)^{1/2},$$

where ρ denotes the constant density of the fluid. All the three cases considered for comparison in the current study, RSC, RC, and SC, were simulated at $\mathrm{Re}_\tau = 400$, where Re_τ is the Reynolds number based on u_τ and half height of the channel.

B. Numerical procedure

The governing equations are the 3D isothermal Navier-Stokes equations for a Newtonian fluid. MGLET, an in-house finite volume solver [13], has been used for solving the equations. The solver uses a second-order central difference scheme for discretizing the convection and diffusion terms. The solution is advanced in time using the second order Adams-Bashforth method. The Poisson equation for pressure is solved by an iterative procedure using the velocity-pressure iteration and the solution is accelerated by a multigrid cycle.

The solution of the flow field is obtained in a staggered Cartesian mesh. In the cases considered here, the mesh is uniform in x and y, while in z, the mesh is uniform from the wall to the plane of rib-crests, beyond which it is modestly stretched toward the channel centerline. The mesh is symmetric about the channel centreline. Table I lists, for RC and RSC, the number of mesh points and the cell spacing in terms of wall units (ν/u_τ). In addition, the ratio of the largest cell dimension to the Kolmogorov length scale, $\Delta_r = \max(\Delta x, \Delta y, \Delta z)/\eta$ are presented, where Δx, Δy, and Δz are the grid cell dimensions in the corresponding directions. In both cases, the maximum values of Δ_r have been reported, which are less than 1. Furthermore, in Fig. 3, the sufficiency of the grid resolution for RSC and RC has been shown, in terms of Grötzbach's criterion [14], which was also

TABLE I. Spatial resolutions used in the simulations of RC and RSC. In both cases, the size of the computational box is $(L_x, L_y, L_z) = (12.8h, 6.4h, 2.0h)$ and that of the grid is $(N_x, N_y, N_z) = (1024, 512, 320)$; the spacings have been normalized using u_{τ_r} and ν. Here Re_m is Reynolds number based on the bulk mean velocity U_m and the channel half-height h, and Δz_c^+ refers to the resolution within the cavity. $^\dagger\Delta_r$ refers to the ratio, $\max(\Delta x, \Delta y, \Delta z)/\eta$ and the maximum values, which in both the cases occur at $z/h \approx 0.1$, have been reported. η is the Kolmogorov length scale.

Case	Re_m	Δx^+	Δy^+	Δz_c^+	$\Delta_r{}^\dagger$
RC	3932	6.1	6.1	1.2	0.56
RSC	4732	5.8	5.8	1.1	0.64

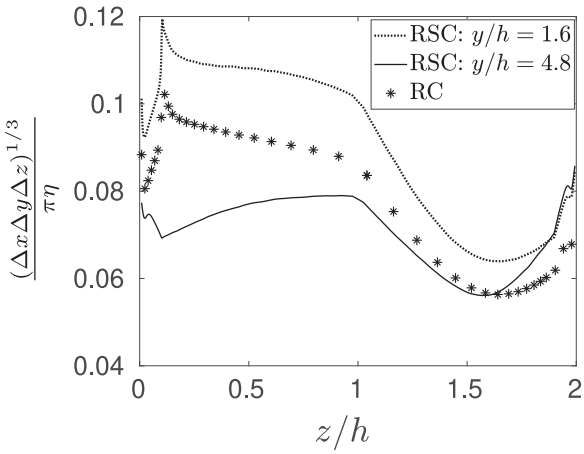

FIG. 3. Grid resolution for RC and RSC, in terms of Grötzbach's criterion [see Eq. (3)]; the variation has been shown along the wall-normal direction.

used by Krogstad *et al.* [15], Ashrafian and Andersson [16], etc. The criterion is given by

$$\frac{(\Delta x \Delta y \Delta z)^{1/3}}{\pi \eta} \leqslant 1.$$

As evident from the figure, the grids of RSC and RC satisfy the Grötzbach's criterion. In the simulations, periodic boundary conditions were assigned along x and y, while the top and the bottom walls and the rib surfaces were supplied with the no-slip and the impermeability conditions.

To validate the numerical method used in the current study, smooth and rough channel flows at different Reynolds numbers have been simulated using MGLET; details of these simulations are listed in Table II. The former is compared with the DNS at $\mathrm{Re}_\tau = 395$ by Abe *et al.* [17], and the latter, with the DNS of rough channel flow at $\mathrm{Re}_{\tau_r} = 260$ by Burattini *et al.* [6], where Re_{τ_r} is based on the friction velocity at the bottom rough wall. Turbulent statistics have been presented in Fig. 4, drawing a comparison between the aforementioned cases. It can be observed that except u_{rms} at $z/h = 1.5$, which has a modest difference, the data compare well with those in the literature.

III. RESULTS AND DISCUSSION

After the flow reached a statistically steady state, the mean quantities, denoted by $\langle\,\rangle$, were obtained by averaging 800 independent samples in time at an interval of k/u_τ. The obtained 3D field was further averaged in x, as is done in the study of Ikeda and Durbin [18] and Burattini *et al.* [6]. Note that the data within the volume of the ribs is excluded from the streamwise average. Since the mean flow in RSC is inhomogeneous in y, two locations along the span—$y/h = 1.6$ on the rough

TABLE II. Computational details of the validation cases, and their corresponding comparison studies from literature. In the case of rough channel-flow simulations, $2H$ is not the channel height, but rather the height from the plane of rib-crests to the top wall of the channel. Re_{τ_r} is based on the bottom wall friction velocity and for smooth cases, $\mathrm{Re}_{\tau_r} = \mathrm{Re}_\tau$.

Comparison cases		$L_x \times L_y \times L_z$	$N_x \times N_y \times N_z$	Re_m	Re_{τ_r}
Smooth	a. Abe *et al.* [17]	$6.4h \times 3.2h \times 2h$	$256 \times 256 \times 192$	6992	395
	b. MGLET		$512 \times 200 \times 320$	7000	400
Rough	a. Burattini *et al.* [6]	$8H \times \pi H \times 2H$	$451 \times 151 \times 193$	2800	260
	b. MGLET		$480 \times 200 \times 328$	2946	243

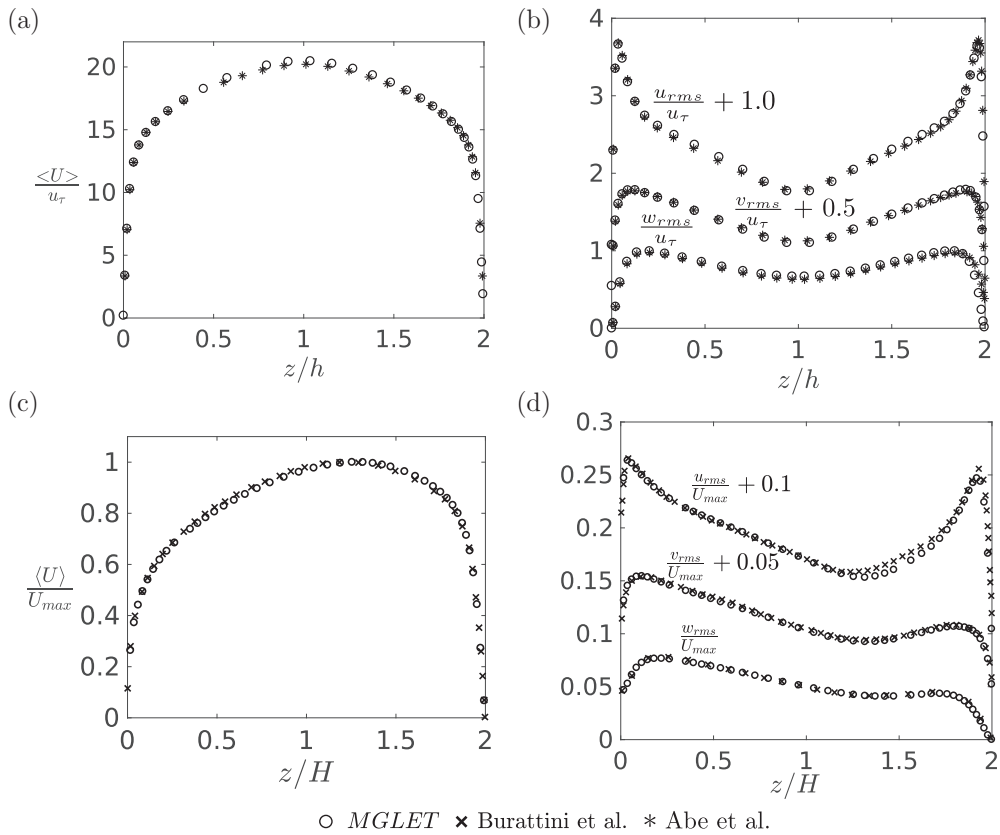

FIG. 4. Profiles of (a), (c) mean streamwise velocity $\langle U \rangle$; (b), (d) RMS of velocity fluctuations, computed using MGLET. Top panel: Profiles from smooth channel DNS at $\mathrm{Re}_\tau = 400$, normalized with the friction velocity u_τ and compared with those from Abe *et al.* [17] at $\mathrm{Re}_\tau = 395$; bottom panel: Profiles from ribbed channel DNS at $\mathrm{Re}_\tau = 260$, normalized with the maximum streamwise velocity $U_{\max}$ and compared with those from Burattini *et al.* [6] at the same Reynolds number. In panels (c) and (d), $z/H = 0$ corresponds to the plane of rib-crests. All the data have been averaged in x and the normalized profiles of u_{rms} and v_{rms} are shifted, in panel (b) by 1.0 and 0.5 and in panel (d) by 0.1 and 0.05, respectively.

side of RSC (also "RSC-rough") and $y/h = 4.8$ on the smooth side (also "RSC-smooth")—were chosen to present both the statistics and the instantaneous data in the (x, z) plane. In the case of RC, the statistics are averaged along homogeneous spanwise direction, while in the case of SC they are averaged along streamwise and spanwise directions. Quantities denoted by a superscript "+," were normalized with ν and the friction velocity—the average one u_τ or the one corresponding to the rib-roughened wall, u_{τ_r}. The normalization variables have been explicitly mentioned for all the quantities presented in this work. In the cases of RSC and RC, only half the extent of the domain in x has been shown for comparisons of instantaneous flow features with those of SC.

A. Mean and instantaneous flow features

Figures 5(a) and 5(b) show the streamline pattern averaged in time and x. The presence of a significant secondary circulation in the form of a pair of counter-rotating roll cells, is strikingly evident from the figure. The mean streamlines display an upward flow at $y/h = 4.8$ and a downwash at $y/h = 2.0$, termed, respectively, the ascending and descending branches of the circulation. The contours of $\langle U \rangle^+$ in Fig. 5(a) show reduced magnitudes at $y/h = 4.8$, up to half-height of the

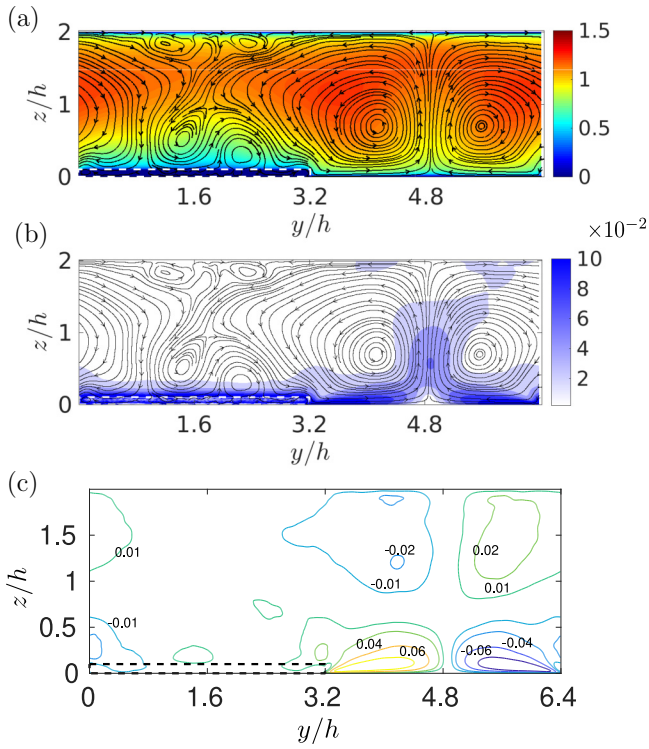

FIG. 5. Contour plots on the (y, z) plane, of (a) mean streamwise velocity $\langle U\rangle/U_m$; (b) $\sqrt{\langle V\rangle^2 + \langle W\rangle^2}/\langle U\rangle$; (c) mean spanwise velocity $\langle V\rangle/U_m$. Contours in panels (a) and (b) are superimposed with the mean secondary streamlines. U_m denotes the bulk mean velocity.

channel, which is consistent with the higher magnitudes of $\sqrt{\langle V\rangle^2 + \langle W\rangle^2}/\langle U\rangle$ there, as shown in Fig. 5(b). Therefore, this reduction in $\langle U\rangle^+$ can plausibly be attributed to the strength of secondary circulation, which can be understood as a hindrance to the streamwise flow. The contours of $\langle V\rangle/U_m$ are presented in Fig. 5(c) for RSC. The presence of the roll-cell pair is clearly visible from the distribution of the contours. Also, the circulation leading to the updraft is much stronger than the return flow at the smooth top wall.

The bulk mean velocities U_m^+ were presented in Table III—the one for RSC evidently falling between the other two. In the case of RSC, the bulk velocities calculated separately from the smooth and rough halves of the channel are 12.32 and 11.64, respectively. It is interesting to note that U_m, estimated from the RSC-smooth is lower than that of SC, and U_m estimated from the RSC-rough is higher than that in RC. The secondary circulation in the (y, z) plane of RSC has enhanced the transfer of momentum from the smooth half region to rough half region and thereby causing a higher U_m in the RSC-rough, compared to that in RC and lower U_m in the RSC-smooth, compared to that in SC.

Figure 6(a) shows the comparison of streamwise velocity profiles from the three cases, normalized with their respective bulk velocities U_m. Unlike in the case of SC, the $\langle U\rangle$ profile from the RSC-smooth is not symmetric about the center line, which is due to the effect of the ascending branch of the mean secondary circulation, hindering $\langle U\rangle$, as shown in Fig. 5(b). A constant slope of $\langle U\rangle/U_m$ profile from RSC-smooth is observed in the core region with $\partial\langle U\rangle/\partial z = 2.88$. Unlike in SC, the positive slope of $\langle U\rangle/U_m$ profile of RSC-smooth is prevalent beyond the half-height of the channel. The constant slope of the mean velocity profile can plausibly be attributed to the total shear stress shown in Fig. 6(c), which is nearly constant up to $z/h = 1.5$. Comparing the

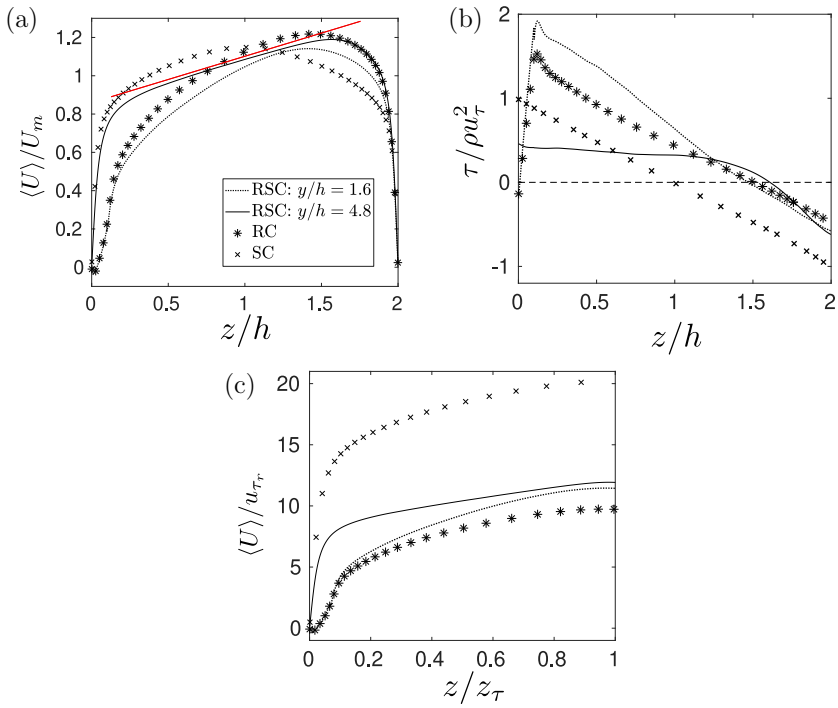

FIG. 6. Mean streamwise velocity normalized with (a) bulk velocity, U_m; (c) friction velocity of rough wall, u_{τ_r} from the corresponding flows. (b) Total shear-stress normalized with u_τ. z_τ in panel (c) denotes the zero-crossing of the shear stress profiles in panel (b). The red dashed line in panel (a) shows slope of the central linear region in the profile from RSC at $y/h = 4.8$.

profile from RSC-rough with that from RC, the peak of the former is shifted toward the center of channel. This can plausibly be attributed to the combined effect of lower drag by the bottom wall of RSC and the transfer of momentum from RSC-smooth to RSC-rough. In spite of being normalized with different U_m, the profiles from RC and RSC-rough have merged up to $z/h = 0.12$. Although, all the profiles from RSC, RC and SC have merged next to the top wall, profiles from RC and RSC-smooth have merged at $z/h = 0.25$ from the top wall. The wall-normal profiles of total shear stress, $\tau(z) = -\rho\langle uw \rangle + \mu\langle \partial U/\partial z \rangle$, for SC, RC, RSC-rough, and RSC-smooth are shown in Fig. 6(b). Profiles of $\tau(z)$ are linear in all the cases, except RSC-smooth. The height from the bottom wall, of the zero-crossing of $\tau(z)$, is denoted by z_τ. In the case of SC, z_τ is half height of the channel, while in the case of RC it is $1.5h$. In the case of RSC, z_τ for RSC-rough and RSC-smooth are 1.46 and 1.6, respectively. The height of z_τ is nearly equal to the height of maximum $\langle U \rangle$ as is evident from Fig. 6(a). A higher z_τ in RSC-smooth can be attributed to the presence of the updraft, causing deepening of the momentum exchange layer in RSC-smooth.

To better understand the effects of the rough wall on the variation of $\langle U \rangle$, it can be scaled with u_{τ_r}, the local friction velocity at the bottom rough wall. In the cases of RC and RSC, u_{τ_r} is given by $u_{\tau_r}^2 = (F_d + P_d)/\rho$, where F_d and P_d are the average skin-friction and form drags, respectively, caused by the bottom rough wall and calculated as shown in equation (3) below. In the case of SC, P_d is zero and the only contribution to the friction velocity comes from F_d. Profiles of streamwise velocity normalized by the scales u_{τ_r} and z_τ from RSC, RC, and SC are presented in Fig. 6(c). In the case of RSC, u_{τ_r} has been obtained from the friction velocities over both rough and smooth halves of the bottom wall as, $u_{\tau_r}^2 = \frac{1}{2}(u_{\tau_r,\text{rough}}^2 + u_{\tau_r,\text{smooth}}^2)$. The profiles are presented up to their respective z_τ. This comparison indicates the drag effect of underlying roughness, which is highest

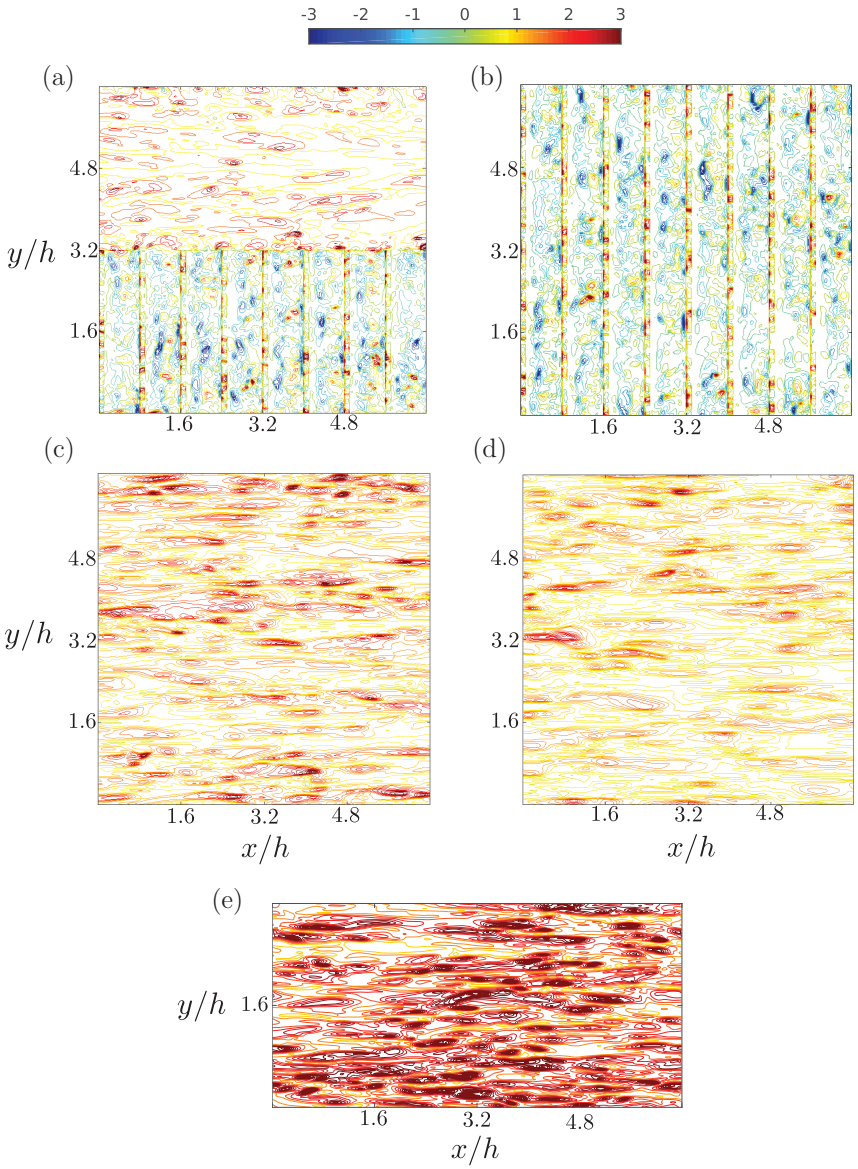

FIG. 7. Contours of instantaneous skin friction coefficient $C_f = \mu \frac{dU}{dz}/(\frac{1}{2}\rho u_\tau^2)$ on the bottom walls of (a) RSC and (b) RC; top walls of (c) RSC and (d) RC; (e) one of the walls of SC.

in the case of RC > RSC: $y/h = 1.6$ > RSC: $y/h = 4.8$ > SC. Also, the nonzero spanwise velocity at the rough-smooth interface depicts the exchange of momentum between the two halves of RSC.

A comparison has been drawn between the three cases for the instantaneous skin friction coefficient C_f plotted on the (x, y) plane. The contours are shown for the bottom and the top walls in Fig. 7. It is evident from Fig. 7 that while both SC and RSC-smooth have positive C_f, the latter has a lower value of C_f indicating a lower velocity gradient, $\frac{\partial \langle U \rangle}{\partial z}$ at its bottom wall. This can be attributed to the enhanced momentum exchange, under the influence of secondary circulation shown in Fig. 5(b). Comparing the contours of C_f in RC to those in RSC-rough, the regions of negative C_f indicate that the recirculation inside the cavity is stronger in the case of RSC-rough. Further, the contours in RSC-rough exhibit sporadic patches of intense C_f, while in the case of RC the contours

TABLE III. Average skin friction coefficient $\overline{C_f}$ and average drag coefficient $\overline{C_d}$ for RSC, RC, and SC. See Eqs. (2) and (3) for the definitions of $\overline{C_f}$ and $\overline{C_d}$. Re_{τ_r} and Re_{τ_s} correspond to Reynolds numbers based on local friction velocities calculated for the bottom and top walls—u_{τ_r} and u_{τ_s}, respectively.

Configuration	U_m/u_τ	Re_{τ_r}	Re_{τ_s}	Wall condition	$\overline{C_f}$	$\overline{C_d}$
RSC	11.8	470	310	Bottom wall, rough half	−0.19	4.58
				Bottom wall, smooth half	1.1	–
				Top smooth wall	1.2	–
RC	9.8	492	276	Bottom rough wall	−0.16	3.19
				Top smooth wall	0.95	–
SC	17.6	400	400	Either smooth wall	2.0	–

are more uniform. This indicates the presence of larger scales of motion in RSC than in RC. Figure 7 indicates the presence of similar streaks on the top walls in RSC, RC and SC, although they differ in terms of magnitude.

In the rough-channel cases, form drag is caused due to the difference in mean pressure between the vertical faces of the ribs. The skin-friction drag and the form drag (per unit span width) averaged for the entire pitch are, respectively,

$$F_d = \frac{1}{\lambda}\int_0^{\lambda}\left(\mu\frac{d\langle U\rangle}{dz_w}\right)dx \quad \text{and} \quad P_d = \frac{1}{\lambda}\int_0^{k}(\Delta P)dz_w, \tag{2}$$

where ΔP is the pressure differential across the ribs and z_w is the away-from-the-wall coordinate, where $z_w = z$ on the bottom wall and $z_w = 2h - z$ on the top wall. The dimensionless counterparts of the drag forces, $\overline{C_f}$ and $\overline{C_d}$, defined, respectively, as

$$\overline{C_f} = \frac{F_d}{\frac{1}{2}\rho u_\tau^2} \quad \text{and} \quad \overline{C_d} = \frac{P_d}{\frac{1}{2}\rho u_\tau^2}, \tag{3}$$

are presented in Table III for the three cases. Comparing RSC-rough to RC, higher inertial effects, $\frac{\partial U}{\partial t} + \frac{(\partial U_i U_j)}{\partial x_j}$ in the former lead to a higher $\overline{C_d}$, leading to a stronger re-circulation of the flow within the cavity, as mentioned earlier. Reynolds numbers based on friction velocities u_{τ_r} and u_{τ_s}, corresponding to bottom and top walls, respectively, are also listed in Table III. The relative contribution of Reynolds stress, $-\langle uw\rangle/u_{\tau_r}^2$ and viscous shear stress, $\mu\langle\frac{\partial U}{\partial z}\rangle/u_{\tau_r}^2$ to the total shear stress, was estimated at the rib crest level for RC as 0.8 and 0.07; for RSC as 0.84 and 0.06, respectively.

B. Turbulence statistics

RMS of velocity fluctuations exhibit higher magnitudes in RSC-rough than in RC, SC and RSC-smooth. This is evident from their streamwise-averaged profiles shown in Fig. 8. Also all the RMS values in RSC-smooth are lower than in SC, except u^+_{rms}, which in the core region of the channel, is higher in RSC-smooth. The flow in RSC-rough manifests higher RMS values than the flow in RSC-smooth. The profiles of v^+_{rms} and w^+_{rms} in RC coincide with their counterparts in SC beyond $z/z_\tau = 0.2$. However, when it comes to u^+_{rms}, the near-wall peak value in SC is higher than those in RSC-rough and RC, while away from the wall, u^+_{rms} is lower in SC. While SC may seem more anisotropic near the wall due to higher values of u^+_{rms} there, the anisotropic nature of the flow can be more accurately presented using the Reynolds stress anisotropy tensor, based on the velocity covariance tensor $\langle u_i u_j\rangle$ as

$$b_{ij} = \frac{\langle u_i u_j\rangle}{\langle u_k\, u_k\rangle} - \frac{1}{3}\delta_{ij}. \tag{4}$$

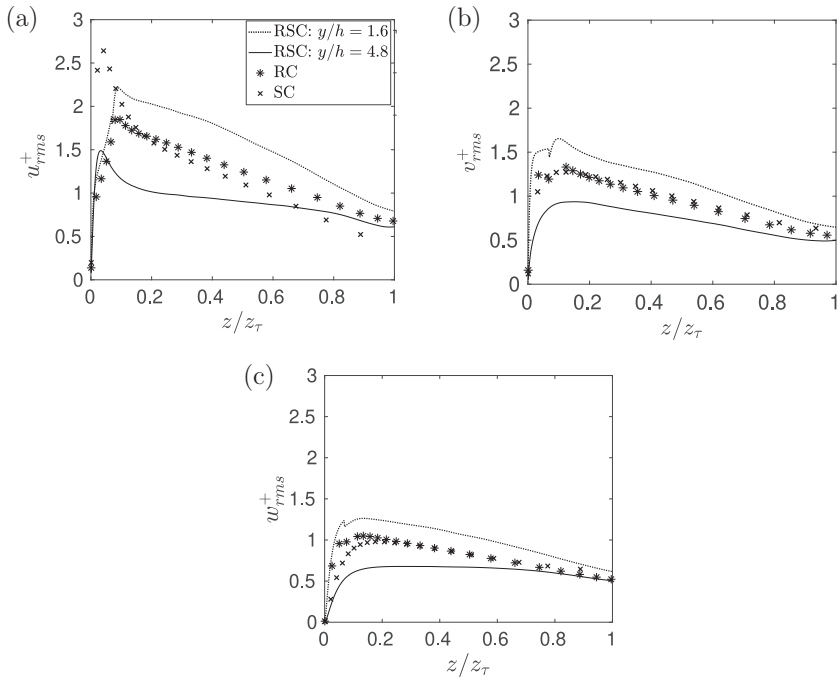

FIG. 8. RMS of velocity fluctuations normalized with the scales u_{τ_r} and z_τ, from RSC, RC, and SC.

b_{ij} aids in the measurement of anisotropy. The diagonal components of b_{ij}, namely b_{11}, b_{22}, b_{33} lie between $-2/3$ and $4/3$ with a zero trace, $b_{ii} = 0$. The variation of the significant components of b_{ij} are presented in Fig. 9. In the study of symmetrically ribbed channel-flows by Varma *et al.* [11], turbulence in the flow, close to the wall, was observed to be more isotropic than that in a smooth channel flow at the same Re_τ. This is also evident from the current comparison of RC (asymmetrically ribbed channel) with SC. The reduction in anisotropy near the wall in RC, as compared to that in SC, is due to the drop in b_{11} and an increase in the spanwise component, b_{22}.

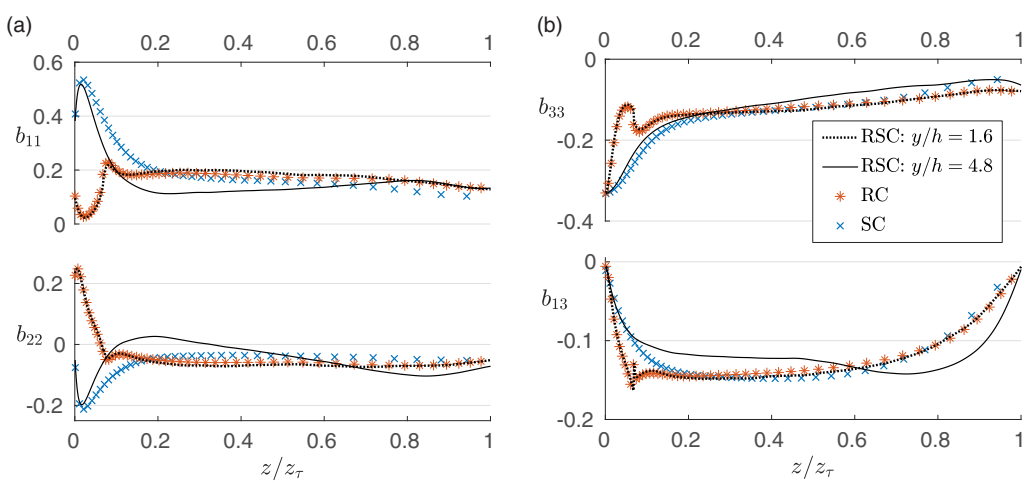

FIG. 9. The variation of nonzero components of the anisotropy tensor, b_{ij} from RSC, RC, and SC.

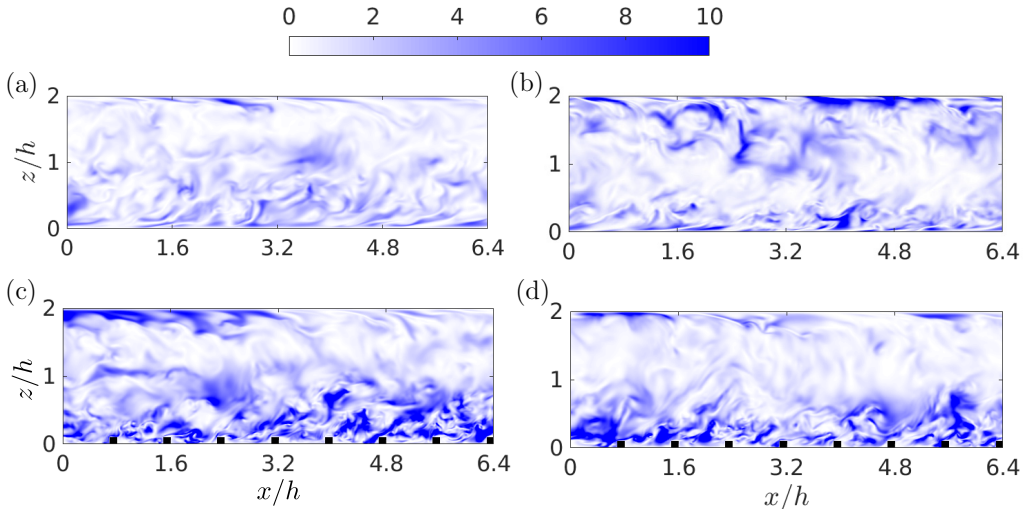

FIG. 10. Instantaneous turbulent kinetic energy normalized with u_τ^2 in the (x, z) plane from (a) RSC-smooth ($y/h = 4.8$); (b) SC ($y/h = 1.6$); (c) RSC-rough ($y/h = 1.6$); (d) RC ($y/h = 3.2$).

In addition, variation of b_{ij} in RSC-rough closely follows that in RC, with the inhomogeneity of the roughness in the former having little effect on b_{ij}. However, b_{ij} does not vary identically, in RSC-smooth and SC, where RSC-smooth shows more isotropic turbulence, especially in the region away from the wall. This nature of RSC-smooth can be attributed to the vertical mixing by the strong updraft at $y/h = 4.8$.

In general, between flows driven by the same pressure gradient, the one with the lower bulk velocity is more turbulent due to the transfer of energy from the mean flow to turbulence. As stated earlier, the bulk velocity of RC is lower than that of RSC. In contrast to this, as evident from the contour plots of instantaneous turbulent kinetic energy ($q^{2^+} = 0.5u_iu_i/u_\tau^2$) in Figs. 10(c) and 10(d), q^2 at $y = 1.6h$, in RSC-rough is more intense than that in RC. Although RSC and RC are driven by the same pressure gradient force, RSC-rough has an additional gain of momentum from its smooth half, when compared to the RC. This additional momentum has caused higher bulk velocity and higher turbulence in the rough half of RSC when compared to RC. In the case of RC, majority of the turbulence is only due to vortex shedding from the underlying ribs, while in the case of RSC-rough, significant q^2 is observed at the top wall, in addition to q^2 at the roughened portion of the bottom wall. The interaction of the secondary circulation with the streamwise flow could be the possible cause of turbulence generated at the top wall of RSC-rough. The above mentioned contradiction between the bulk velocity and turbulence is also observed between RSC-smooth and SC, where the former is of lower bulk velocity and less turbulent than the latter, as shown in Figs. 10(a) and 10(b). This further confirms the idea that the lower bulk velocity observed in RSC-smooth as compared to that of SC is solely due to hindrance caused by the secondary circulation in RSC. In other words, the lower bulk velocity in RSC-smooth, compared to that of SC, is due to the loss of momentum to its rough half.

To further understand the distribution of q^2, the production rate of TKE ($=\langle q^2\rangle$), P_k is investigated, which is given by

$$P_k = -\langle u_i u_j\rangle \frac{\partial \langle U_i\rangle}{\partial x_j}, \tag{5}$$

where u_i represents the fluctuating velocities. The profiles of P_k^+ shown in Fig. 11(a) (P_k normalized with $u_{\tau_r}^4/\nu$) from RSC-rough and RSC-smooth merge just above the center of the channel, *viz* at

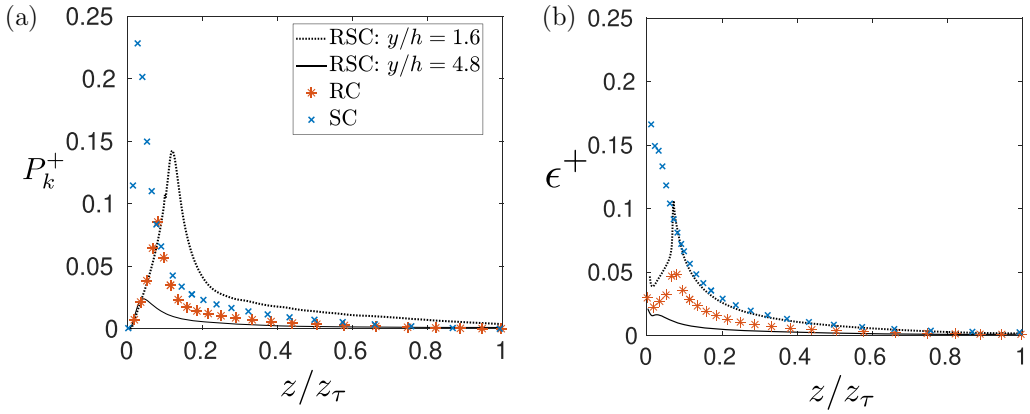

FIG. 11. Variation of (a) production rate P_k^+ and (b) dissipation rate ϵ^+, of turbulent kinetic energy in RSC, RC, and SC. The data have been normalized with $u_{\tau_r}^4/\nu$.

$z/z_\tau = 1$. In RC and RSC-rough P_k^+ remains positive up to the channel centerline, while in RSC-smooth, P_k^+ drops to zero much closer to the rough wall and stays flat for a greater extent in the channel core. Similar to the comparison of $u_{\rm rms}^+$ the P_k^+ of SC is higher than that of RSC-rough in the near-wall region, while away from the wall, P_k^+ of SC is lower than RSC-rough for a greater extent of the channel. Comparing between RSC-rough and RC, the P_k^+ profile of the former is higher than that of the latter throughout the vertical extent of $z/z_\tau = 1$. P_k of RSC-smooth is lower than that of SC, RC, and RSC-rough. The profiles of P_k^+ from RSC and SC are in agreement with the instantaneous TKE shown in Figs. 10(a) and 10(b). The relative magnitudes of P_k^+ are similar to those of q^{2+}—the magnitudes are higher in RSC-rough than those in RC and the magnitudes in RSC-smooth are lower than those seen in SC.

The dissipation rate of TKE, ϵ is investigated, which is given by

$$\epsilon = 2\nu\left\langle \frac{\partial u_i}{\partial x_k}\frac{\partial u_i}{\partial x_k}\right\rangle. \tag{5}$$

The profiles of dissipation rate, ϵ^+ (ϵ nondimensionalized by $u_{\tau_r}^4/\nu$) are shown in Fig. 11(b). As evident from the figure, ϵ^+ in SC is higher than that in RSC and RC. Although P_k^+ of SC is higher than that of RC, due to a significantly higher ϵ^+ of SC, the RC is more turbulent than SC, which is also evident from the comparison of instantaneous TKE in Figs. 10(b) and 10(d), and the RMS of velocity fluctuations in Fig. 8. Similar to the comparisons of P_k^+, the ϵ^+ of RSC-rough is higher than that of RC and the ϵ^+ of RSC-smooth is lower than that of SC.

C. Vorticity characteristics

The instantaneous spanwise vorticity ω_y from RSC, RC, and SC have been shown in Fig. 12. Comparing RSC-smooth with that of SC, it can be observed that ω_y in the former is less intense than that in the latter. The ascending branch enhances the exchange of momentum in z, especially in the region close to the top wall. This vertical mixing curbs the velocity gradient $\partial U/\partial z$ and therefore causes ω_y to be less intense in RSC-smooth. Vorticity contours from RSC-rough have been compared to those of RC in Figs. 12 and 14, for ω_y and the streamwise vorticity fluctuations ω_x', respectively. Both ω_y and ω_x' in RSC-rough are higher than those in RC. This can be attributed to the shear developed between the upward flow arising from the ribs and downward flow from the descending branch of the secondary circulation in RSC. It is due to the same reason that ω_x' in the vicinity of the ribs in RSC-rough is more intense than in the smooth half. Further to the comparison of instantaneous vorticity, the magnitude of the mean vorticity $|\langle\omega\rangle| = \sqrt{\langle\omega_x\rangle^2 + \langle\omega_y\rangle^2 + \langle\omega_z\rangle^2}$ is

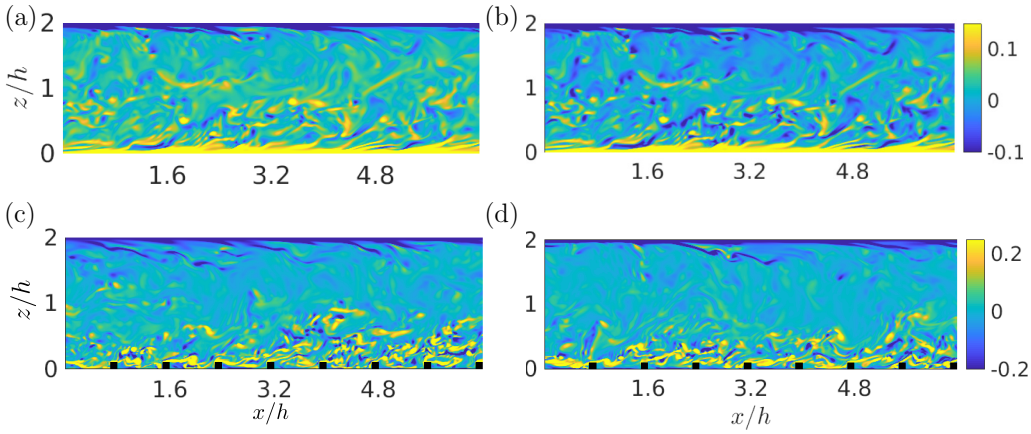

FIG. 12. Instantaneous spanwise vorticity, normalized with u_τ^2/ν, $\langle\omega_y\rangle^+$ in the (x, z) plane from (a) RSC-smooth ($y/h = 4.8$); (b) SC ($y/h = 1.6$); (c) RSC-rough ($y/h = 1.6$); (d) RC ($y/h = 3.2$).

compared for RSC, RC, and SC in Fig. 13. The logarithmic scale is considered to focus on the near-wall region. The comparison of $|\langle\omega\rangle|^+$ is similar to that of ω_y^+ *viz*, higher vorticity in RSC-rough than in RC and lower vorticity in RSC-smooth than in SC. In addition to vortices being shed from the spanwise oriented (lateral) edges, in the case of RSC, there is an additional vortex shedding within the rib-height, from the vertical edges of the ribs at $y/h = 3.2$, as shown in Fig. 15(a). The $\omega_z'^+$ contours indicate that the vortices formed at the leading vertical edge drift toward the smooth half of the channel. Elongated bands of positive and negative $\omega_z'^+$, present abreast, are observed reaching up to $y/h = 4.8$. The bands of $+/-\omega_z'^+$ is similar to what is observed by Leonardi *et al.* [4], with a channel configuration same as RC but with $\lambda/k = 39$. It was stated that the vorticity tubes arising from the leading edge of the ribs appear increasingly aligned with the downstream distance from edge. But this coherence is disrupted by the subsequent ribs in the current case with a smaller λ/k, which is evident from the RSC-rough in Fig. 15. The absence of such elongated bands of $\omega_z'^+$ in RSC-smooth [Fig. 15(b)] indicate that the influence of the vertical edges is limited to rib-height, which is unlike the lateral edges of ribs.

As proposed by Jeong and Hussain [19], the cores of the vortical structures can be visualized using the isosurfaces of $\lambda_2 < 0$, where λ_2 is basically the median of the three eigenvalues of the symmetric tensor $S_{ik}S_{kj} + \Omega_{ik}\Omega_{kj}$. Here, S_{ij} and Ω_{ij} denote the strain-rate and the rotation-rate

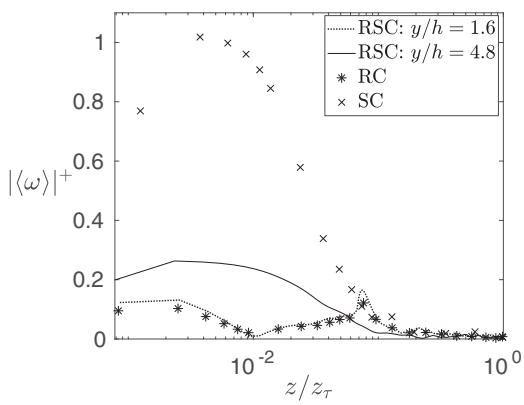

FIG. 13. Profiles of $|\langle\omega\rangle| = \sqrt{\langle\omega_x\rangle^2 + \langle\omega_y\rangle^2 + \langle\omega_z\rangle^2}$, normalized with $u_{\tau_r}^2/\nu$, $|\langle\omega\rangle|^+$ on a logarithmic scale.

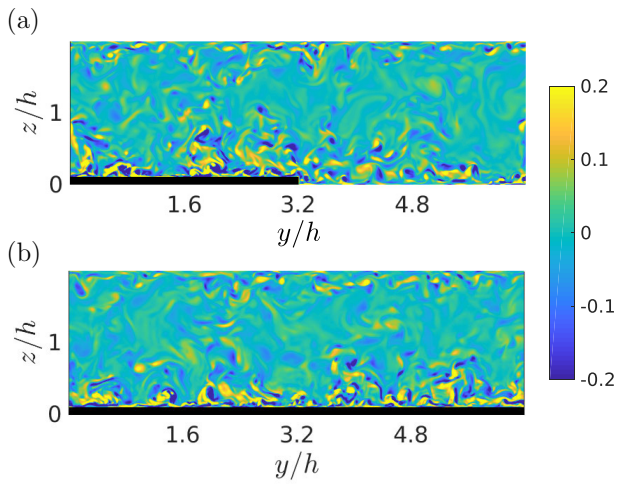

FIG. 14. Streamwise vorticity fluctuation, normalized with u_τ^2/ν, $\omega_x'^+$ in the (y, z) plane at a midrib location, at $x/h = 1.55$ from (a) RSC and (b) RC.

tensors, respectively. Figure 16 depicts the isosurfaces of $\lambda_2 = -0.14$ from RSC and RC. Due to the minimal turbulence in RSC-smooth, there are no vortical structures with $\lambda_2 = -0.14$. Therefore, isosurfaces of a lower magnitude of λ_2 viz. $\lambda_2 = -0.02$ are considered for RSC-smooth and are compared with those from SC, as shown in Fig. 17. In SC, RSC-rough and RC, structures are mostly aligned in the streamwise direction. Compared to RC, the vortical structures in RSC-rough are more dense and are at a higher height. In comparison to RC, the higher streamwise velocity in RSC-rough causes a more intense upward rising flow and thereby drifting the structures to higher heights. The vortical structures emerging from the underlying surface of RSC-smooth, especially in the region of $y/h = 4.8$, are fewer in number and are of smaller spatial extent when compared to those from SC which appear as streamwise elongated tubelike structures. In SC, due to the absence of any obstruction, the vortical structures are elongated to a larger length compared to those from RSC. The low density of structures at $y/h = 4.8$ of RSC is due to the hindrance caused by the secondary roll cell. This is in par with the observation that the flow in RSC-smooth is less turbulent than the

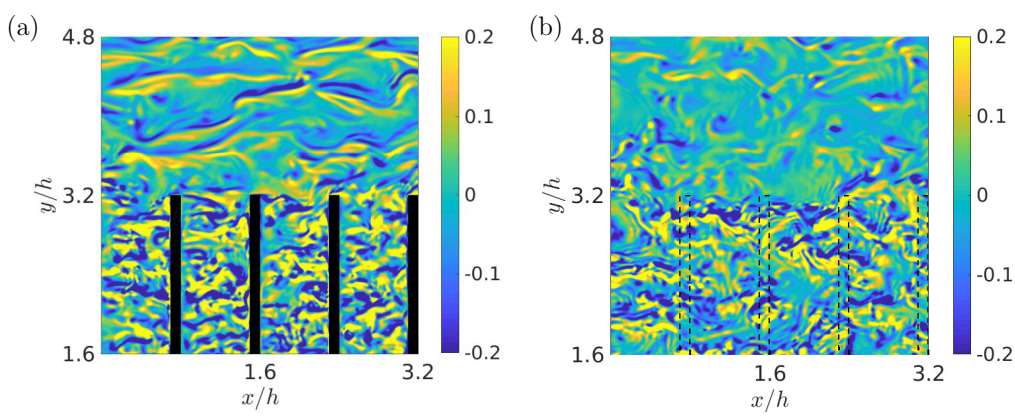

FIG. 15. Wall-normal vorticity fluctuation normalized with u_τ^2/ν, $\omega_z'^+$ in the (x, y) plane at (a) $z/h = 0.1$ and (b) $z/h = 0.2$ from RSC. The data has been presented for only half the span and one-fourth of the streamwise extent.

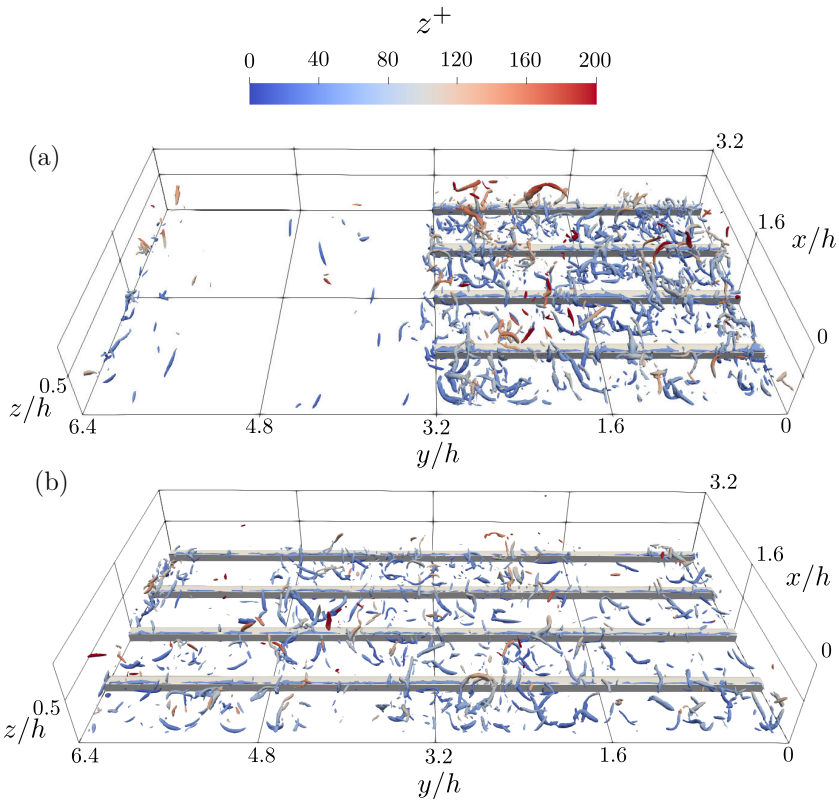

FIG. 16. Isosurfaces of $\lambda_2 = -0.14$ colored with z^+, extending up to $z/h = 0.5$, from (a) RSC and (b) RC.

flow in SC (Fig. 10). In addition, intrusion of structures from the rough half to the smooth half of RSC is observed at heights above $z^+ = 100$. In comparison to RSC and RC, the vortical structures in symmetrically roughened channel flows [11], extend farther from the walls, reaching up to the core of the channel. Also, in the study by Varma *et al.* [11], considerable number of vortical structures,

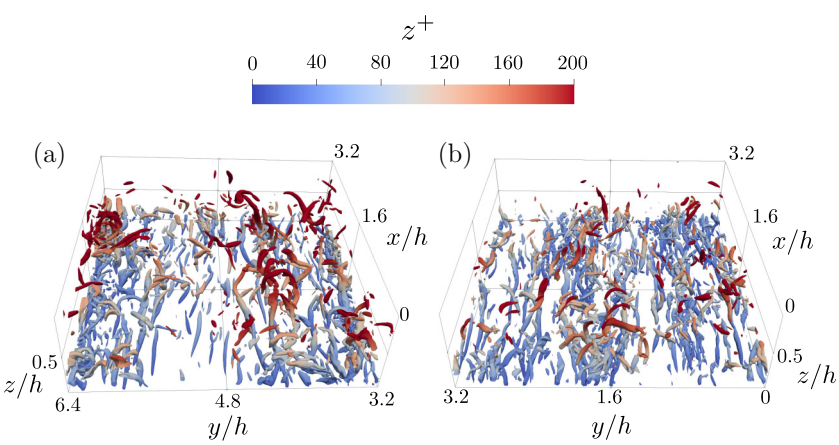

FIG. 17. Isosurfaces of $\lambda_2 = -0.02$ colored with z^+, extending up to $z/h = 0.5$ from (a) RSC-smooth and (b) SC.

TABLE IV. Comparison of maximum height up to which vortical structures are scattered in RSC, RC, and symmetrically roughened channel flows at $\mathrm{Re}_\tau = 180$ and 400 [11].

Case	U_m	z^+
Symmetrically roughened, $\mathrm{Re}_\tau = 400$	6.32	250
Symmetrically roughened, $\mathrm{Re}_\tau = 180$	7.1	130
RC, $\mathrm{Re}_\tau = 400$	8.2	120
RSC, $\mathrm{Re}_\tau = 400$	12	100

with $\lambda_2 = -0.03$, are aligned in the spanwise direction, which is not observed in RSC and RC. It is interesting to observe that, with the increase in U_m of the rough channel flow, the vortical structures are limited to a smaller vertical extent, which is evident from the comparison among RSC, RC, and symmetrically roughened channel flows at $\mathrm{Re}_\tau = 180$ and 400 (see Table IV). This typifies the inertial effect of the streamwise flow, which is inhibiting the upward flow from the ribs and thereby limiting the vortical structures to a lower height.

Figure 18 shows the isosurfaces of positive enstrophy production rate with $\omega_i S_{ij} \omega_j^+ = 0.07$ and 0.035 from RSC and RC, respectively. The positive $\omega_i S_{ij} \omega_j^+$ in RSC is nearly two times that of RC. In the case of RSC, about 34% of the total enstrophy production rate ($\omega_i S_{ij} \omega_j > 0$) is contained within 1% of the total data, which exceeds this threshold of $\omega_i S_{ij} \omega_j^+ = 0.07$. These details are

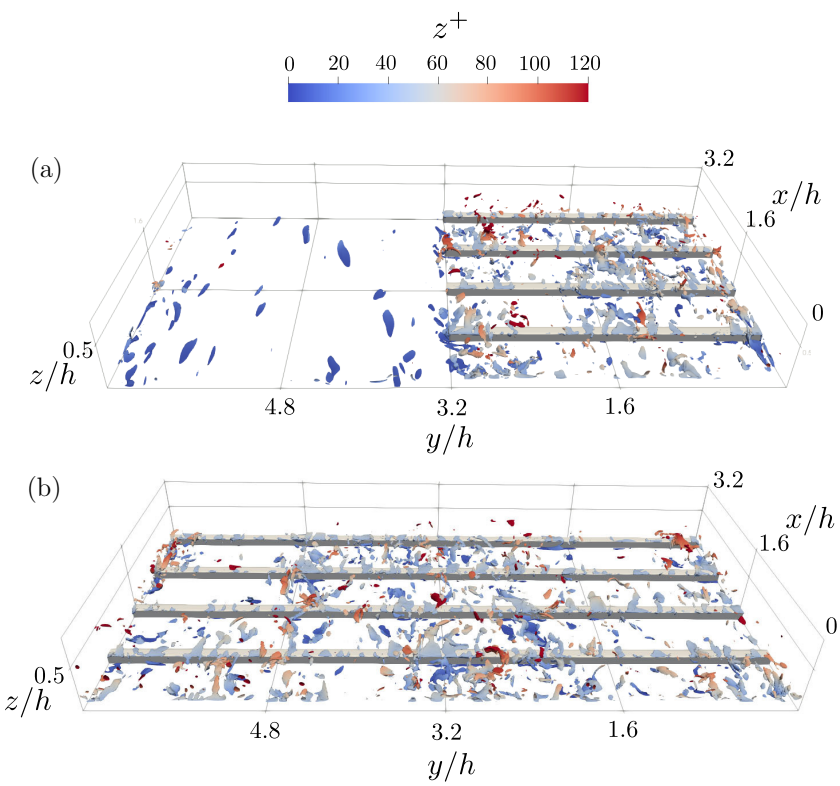

FIG. 18. Isosurfaces of positive enstrophy production rate, $\omega_i S_{ij} \omega_j^+ = \omega_i S_{ij} \omega_j / (\frac{u_{\tau_r}^2}{\nu})^3$ colored with z^+, in the proximity of the ribs in (a) RSC, $\omega_i S_{ij} \omega_j^+ = 0.04$; (b) RC, $\omega_i S_{ij} \omega_j^+ = 0.02$. The domain has been shown only for one-fourth of the extent in x.

TABLE V. Proportions of positive and negative enstrophy production regions with the chosen nominal thresholds for the cases of RSC and RC.

	Positive production rate, $\omega_i S_{ij} \omega_j^+ > 0$			Negative production rate, $\omega_i S_{ij} \omega_j^+ < 0$		
Case	Threshold value, T_+	% data above T_+	$\frac{\omega_i S_{ij} \omega_j^+ > T_+}{\omega_i S_{ij} \omega_j^+ > 0} \times 100\%$	Threshold value, T_-	% data below T_-	$\frac{\omega_i S_{ij} \omega_j^+ < T_-}{\omega_i S_{ij} \omega_j^+ < 0} \times 100\%$
RSC	0.07	1	34	-15.6×10^{-3}	2	46
RC	0.035	1	32	-6.25×10^{-3}	2	49

depicted in Table V for RSC and RC. In both RSC and RC, the majority of the isosurfaces of $\omega_i S_{ij} \omega_j > 0$ are observed on the surface of the ribs and are topologically "sheetlike." A moderate number of these structures from RC are observed above the rib height whose overall topology is a combination of weakly "sheet-forming" and "tube-forming." Compared to RSC-rough, negligible amount of vortex stretching is observed in its smooth half.

The magnitude of negative enstrophy production rate in RSC is of an order higher than that in RC. Figure 19 shows the isosurfaces with $\omega_i S_{ij} \omega_j^+ = -15.6\times10^{-3}$ and -6.25×10^{-3} from RSC and RC, respectively. In both RSC and RC, the isosurfaces of $\omega_i S_{ij} \omega_j < 0$ do not have any distinct shape.

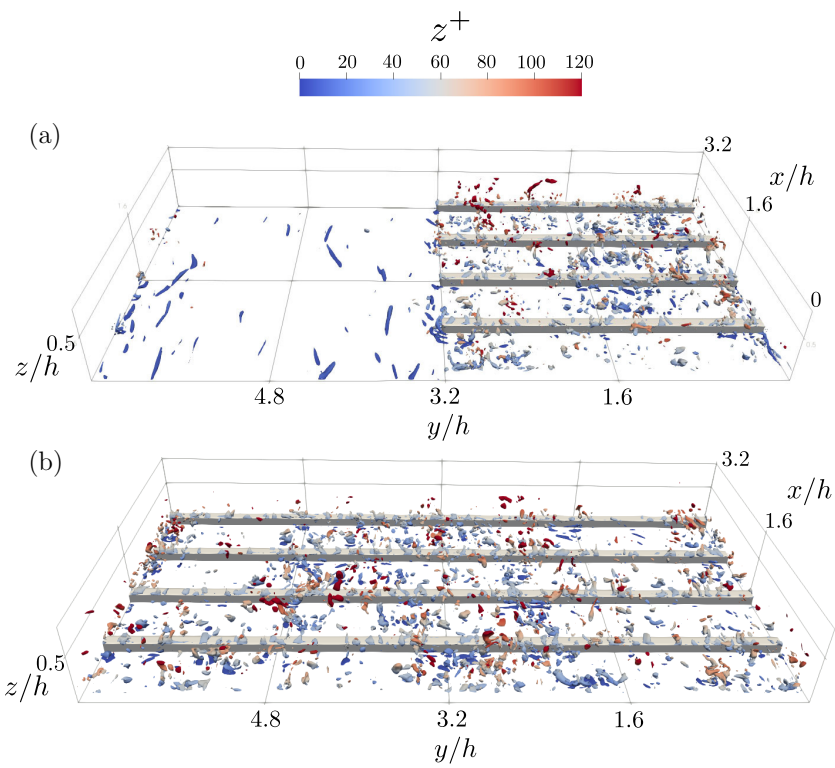

FIG. 19. Isosurfaces of negative enstrophy production rate, $\omega_i S_{ij} \omega_j^+ = \omega_i S_{ij} \omega_j / (\frac{u_{\tau_r}^2}{\nu})^3$ colored with z^+, in the proximity of the ribs in (a) RSC, $\omega_i S_{ij} \omega_j^+ = -9.74\times10^{-3}$; (b) RC, $\omega_i S_{ij} \omega_j^+ = -3.35\times10^{-3}$. The domain has been shown only for one-fourth of the extent in x.

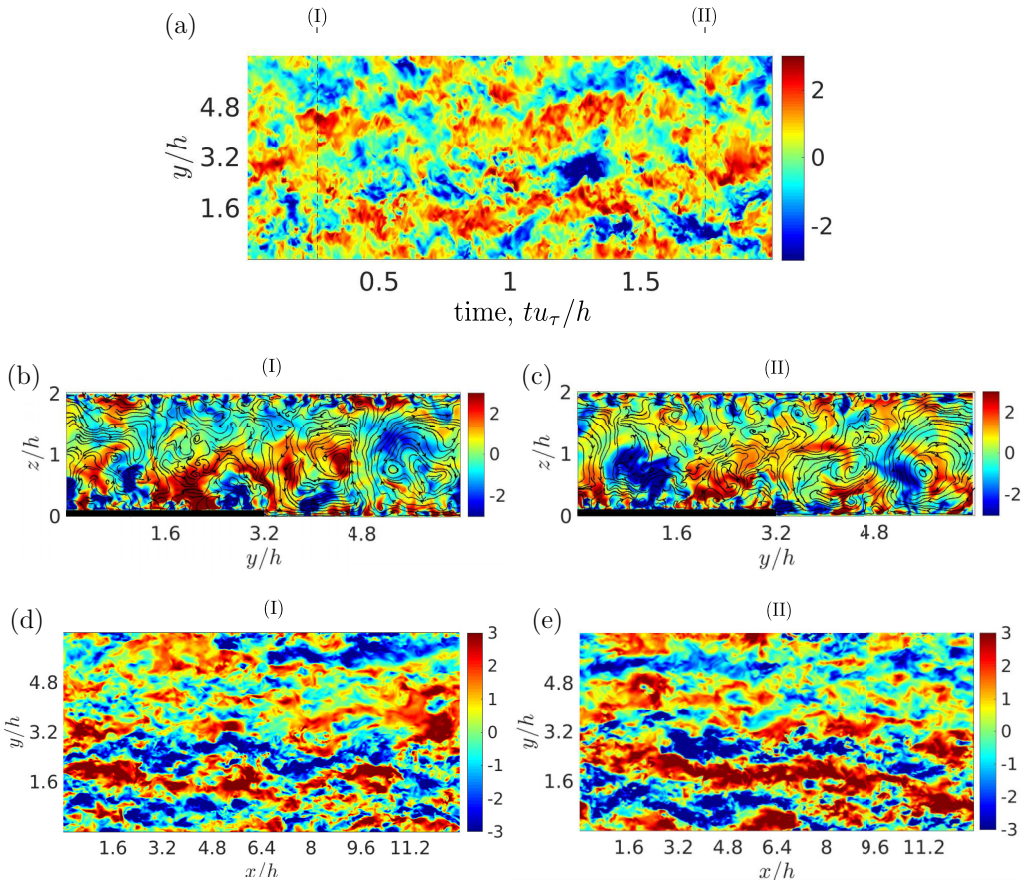

FIG. 20. Variation of the streamwise velocity fluctuation u in RSC. (a) Time traces of u obtained from the spanwise points at the midchannel $z/h = 1$ at a midrib location; (b), (c) Contours of u in (y, z) planes obtained from instants (I) and (II), respectively; (d), (e) Contours of u in (x, y) planes at $z/h = 0.5$ obtained from instants (I) and (II), respectively. The streamlines in panels (b) and (c) were obtained by averaging instantaneous data in (y, z) planes cutting the ribs.

In both RSC and RC, vortex stretching is more prevalent than vortex compression, which is in accordance with Taylor [20], who originally proved that the net value of $\omega_i S_{ij} \omega_j$ is positive. In the DNS studies of rough channel flow by Varma *et al.* [11] and axisymmetric jet flow by Buxton and Ganapathisubramani [21], the tubelike vortical structures were observed to be closely associated with the regions of intense vortex stretching. Therefore, in the current study, the tubelike shape of vortical structures from both RSC and RC, shown in Fig. 16 can be attributed to the prevalence of vortex stretching. Comparing RSC and RC, although the intensity of vortex stretching is higher in the former, the magnitude of its vortex compression is of an order higher than in the latter. This could be the cause of smaller spatial extent of the vortical structures in RSC, compared to those in RC as shown in Fig. 16.

D. Spatiotemporal characteristics

The time traces of streamwise velocity fluctuation u are presented in Fig. 20(a) for a nondimensional time of $2tu_\tau/h$; the data are obtained from all the spanwise points at the channel centerline and at a midrib location. In addition, contour plots of u in (y, z) and (x, y) planes have been presented

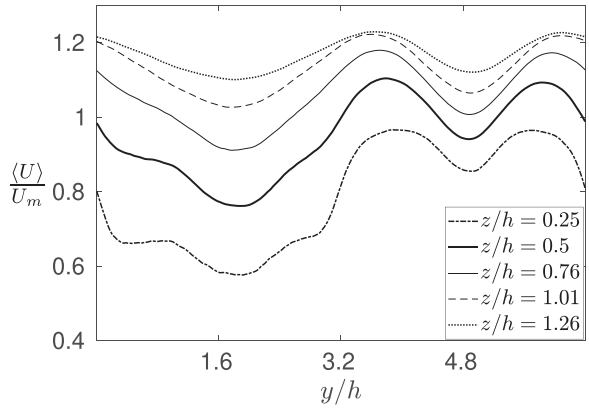

FIG. 21. Spanwise variation of the pitch-averaged mean streamwise velocity $\langle U \rangle$, at the midrib location at different wall-normal locations z/h. The velocity data is normalized by the bulk velocity U_m.

for the time instants (I) and (II). The (y, z)-planar plots presented in Figs. 20(b) and 20(c) are shown overlapped with secondary-streamline patterns obtained by averaging the instantaneous streamlines over (y, z) planes passing through the ribs, exempting those within the cavities. The time traces exhibit paired regions of positive and negative u in both rough and smooth halves of RSC. In

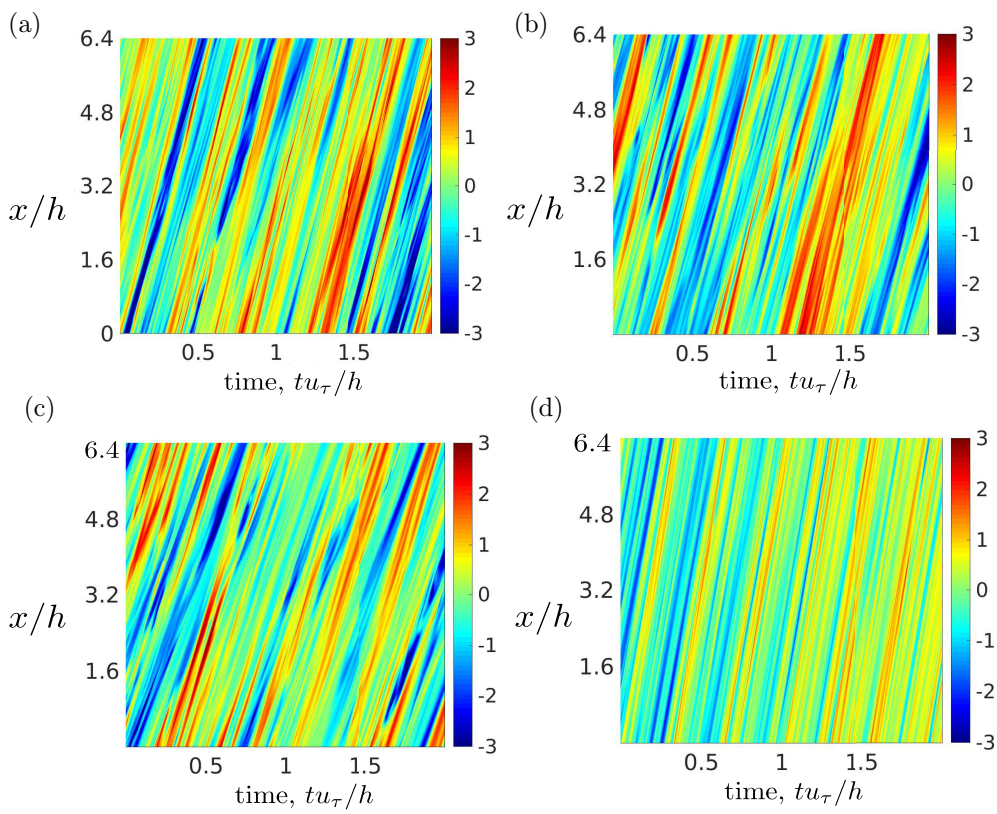

FIG. 22. Time traces of streamwise velocity fluctuation u along the x direction at $z/h = 1.0$ in (a) RSC-rough ($y/h = 1.6$); (b) RSC-smooth ($y/h = 4.8$); (c) RC ($y/h = 3.2$); (d) SC ($y/h = 1.6$). In the case of RC and RSC, the data has been presented up to only half the extent in x.

accordance with this, the distributions of u in Figs. 20(b) and 20(c) display regions of alternating positive and negative u along the span of the channel, which is prominent in the bottom half of the channel. The instantaneous streamlines at time instants (I) and (II) indicate the presence of a pair of counter-rotating roll cells extending across the smooth-half of RSC.

The intense fluctuations in u in the bottom half of RSC, can also be observed in (x, y) planes at $z/h = 0.5$, presented in Figs. 20(d) and 20(e), for the time instants (I) and (II), respectively. The flow exhibits streamwise-elongated velocity streaks, where the high- and low-speed streaks situated side-by-side, demonstrate a wavelike form. Similar to that in the study by Teja *et al.* [10], this oscillation in u can be attributed to the presence of a shear-layer instability at the interface of the rough half and the smooth half of RSC. Due to the presence of roughness, the streamwise velocity in the rough half of RSC is lower than that in the smooth half, leading to the formation of a shear layer at the interface, as shown in Fig. 21. As depicted in the figure, at the interface, $\partial\langle U\rangle/\partial y$ decreases with the wall-normal height. Also, a linear spanwise variation of $\langle U\rangle$ is observed in the interface region, from profiles at height $z/h = 0.76$ and above. The time traces of u are presented in Fig. 22 for a nondimensional time of $2tu_\tau/h$; the data is obtained along x at the channel centerline. The angle exhibited by the trace of u indicate the local instantaneous streamwise velocity, which is highest in SC and lowest in RC. In the case of SC, the traces of u are consistent over time, while in case of RSC and RC they are broken or inconsistent. The inconsistency can be attributed to the influence of ribs which is highest in RC $>$ RSC: $y/h = 1.6$ $>$ RSC: $y/h = 4.8$.

IV. CONCLUSIONS

The current study investigates the turbulent flow through a channel where one of its walls is mounted transversely with square ribs, spaced at a constant pitch in the streamwise direction. In the first case, the ribs span the entire width of the channel (2D roughness, called RC), while in the second case, the ribs extend to only half the span-width (RSC-rough) leaving the other half smooth (RSC-smooth), leading to a 3D roughness pattern. Direct numerical simulations were performed and the effects of the 3D roughness configuration on the instantaneous and mean quantities were compared to those of the 2D configuration. The height of the ribs is one-tenth of the half-height of the channel and their pitch distance is eight times their height. The flow was set to a Reynolds number, $\mathrm{Re}_\tau = 400$ through the imposed pressure gradient.

In terms of the estimated bulk velocities U_m, the cases compare as follows: RC $<$ RSC $<$ SC; however, the relative contributions to U_m from RSC-smooth and RSC-rough are almost the same. Secondary roll cells are observed in instantaneous and mean streamlines in the (y, z) plane of RSC, where the two counter-rotating roll cells occupy the entire spanwise extent of RSC-smooth. Due to the presence of an intense secondary circulation in RSC-smooth, a region of reduced magnitude of mean streamwise velocity $\langle U\rangle$ has developed there. The profile of $\langle U\rangle$ from RSC-smooth (at $y/h = 4.8$) displays a constant slope in the core of the channel. A lateral shear layer is formed between lower velocity flow of RSC-rough and higher velocity flow of RSC-smooth. The magnitude of this shear decreases with increase in wall-normal height. The time trace and spatial distributions of the streamwise velocity fluctuation displayed a meandering behavior of the low and the high speed streaks.

The RMS velocity fluctuations in RSC were found to be higher on the rough half and a comparison with RC and SC, revealed that RSC-rough is more turbulent than RC, while RSC-smooth is less turbulent than SC. It is noteworthy that RSC-rough while being more turbulent than RC, ironically also has higher U_m than the latter. This has been attributed to the transfer of momentum from the smooth half of RSC to its rough half. Although the anisotropic behavior of the flow in RSC-rough is same as that of RC, the flow in RSC-smooth was observed to be more isotropic compared to the flow in SC. This nature of RSC-smooth is plausibly due to the vertical mixing by the strong updraft at $y/h = 4.8$. The production rate of turbulent kinetic energy P_k, while being prevalent only up to a few rib-heights, is significantly higher on the rough side of RSC as compared to RSC-smooth. Due to a significantly higher dissipation of TKE in SC than that in RC, RC is more turbulent than SC despite

the higher P_k of SC. Under the influence of secondary roll cells, more intense vorticity is observed in RSC-rough than in RC. Unlike RC, an additional vortex shedding is observed in RSC, from the vertical edges of ribs, at the rough-smooth interface. The vorticity generated from these vertical edges drift toward RSC-smooth and appear as pairs of elongated bands of positive and negative $\omega_z'^{+}$ in (x, y) plane. The absence of any obstruction in RSC-smooth has facilitated the formation of such elongated bands of vorticity. The isosurfaces of λ_2 reveal that the vortical structures in RSC-rough are shorter and more slender than those in RC, which is attributed to the higher vortex compression observed in the former. The presence of streamwise elongated vortical structures in all the cases is a result of dominant vortex stretching ($\omega_i S_{ij} \omega_j > 0$). Compared to SC, the vortical structures in RSC-smooth appear to be disrupted, with no distinct shape, under the influence of secondary roll cells.

The DNS data that support the findings of this study are available from the corresponding author upon reasonable request.

ACKNOWLEDGMENTS

The work has received support from the P. G. Senapathy Center for Computing Resource, IIT Madras, through a grant of computing time. In addition, authors acknowledge the Director of National Atmospheric Research Laboratory for the high-performance computing facility, PARAM AMBAR, used for performing the simulations presented in this study.

Authorship statement. Harish Varma and Karthikeyan Jagadeesan contributed equally to this work.

Author Declaration. The authors have no conflicts to disclose.

[1] D. Willingham, W. Anderson, K. T. Christensen, and J. M. Barros, Turbulent boundary layer flow over transverse aerodynamic roughness transitions: Induced mixing and flow characterization, Phys. Fluids **26**, 025111 (2014).

[2] P. Orlandi, S. Leonardi, and R. Antonia, Turbulent channel flow with either transverse or longitudinal roughness elements on one wall, J. Fluid Mech. **561**, 279 (2006).

[3] H. L. Bai, Kevin, N. Hutchins, and J. P. Monty, Turbulence modifications in a turbulent boundary layer over a rough wall with spanwise-alternating roughness strips, Phys. Fluids **30**, 055105 (2018).

[4] S. Leonardi, P. Orlandi, L. Djenidi, and R. A. Antonia, Structure of turbulent channel flow with square bars on one wall, Int. J. Heat Fluid Flow **25**, 384 (2004).

[5] P. Orlandi and S. Leonardi, DNS of turbulent channel flows with two-and three-dimensional roughness, J. Turbul. **7**, N73 (2006).

[6] P. Burattini, S. Leonardi, P. Orlandi, and R. A. Antonia, Comparison between experiments and direct numerical simulations in a channel flow with roughness on one wall, J. Fluid Mech. **600**, 403 (2008).

[7] R. Mejia-Alvarez, J. M. Barros, and K. T. Christensen, Structural attributes of turbulent flow over a complex topography, in *Coherent Flow Structures at Earth's Surface*, edited by J. G. Venditti, J. L. Best, M. Church, and R. J. Hardy (John Wiley & Sons, New York, NY, 2013), pp. 25–41.

[8] R. J. Adrian, C. D. Meinhart, and C. D. Tomkins, Vortex organization in the outer region of the turbulent boundary layer, J. Fluid Mech. **422**, 1 (2000).

[9] V. D. Narasimhamurthy, S. A. Ellingsen, and H. I. Andersson, Bilateral shear layer between two parallel Couette flows, Phys. Rev. E **85**, 036302 (2012).

[10] K. M. Teja, V. D. Narasimhamurthy, H. I. Andersson, and B. Pettersen, Onset of shear-layer instability at the interface of parallel Couette flows, Int. J. Heat Fluid Flow **89**, 108786 (2021).

[11] H. Varma, K. Jagadeesan, V. D. Narasimhamurthy, A. P. Kesarkar, and H. I. Andersson, LES and DNS of symmetrically roughened turbulent channel flows, Acta Mech. **232**, 4951 (2021).

[12] B. R. Morton, The generation and decay of vorticity, Geophys. Astrophys. Fluid Dyn. **28**, 277 (1984).
[13] M. Manhart, A zonal grid algorithm for DNS of turbulent boundary layers, Comput. Fluids **33**, 435 (2004).
[14] G. Grötzbach, Spatial resolution requirements for direct numerical simulation of the Rayleigh-Bénard convection, J. Comput. Phys. **49**, 241 (1983).
[15] P. Å. Krogstad, H. I. Andersson, O. M. Bakken, and A. Ashrafian, An experimental and numerical study of channel flow with rough walls, J. Fluid Mech. **530**, 327 (2005).
[16] A. Ashrafian and H. I. Andersson, Roughness effects in turbulent channel flow, Prog. Comput. Fluid Dyn., Int. J. **6**, 1 (2006).
[17] H. Abe, H. Kawamura, and Y. Matsuo, Direct numerical simulation of a fully developed turbulent channel flow with respect to the Reynolds number dependence, J. Fluids Eng. **123**, 382 (2001).
[18] T. Ikeda and P. A. Durbin, Direct simulations of a rough-wall channel flow, J. Fluid Mech. **571**, 235 (2007).
[19] J. Jeong and F. Hussain, On the identification of a vortex, J. Fluid Mech. **285**, 69 (1995).
[20] G. I. Taylor, Production and dissipation of vorticity in a turbulent fluid, Proc. R. Soc. London, Ser. A **164**, 15 (1938).
[21] O. R. H. Buxton and B. Ganapathisubramani, Amplification of enstrophy in the far field of an axisymmetric turbulent jet, J. Fluid Mech. **651**, 483 (2010).